



Photoactive cobalt-bipyridine electron mediator promotes reversible Li_2O_2 formation in irradiated Li-O₂ battery

Xinjian Li^{a,b,1}, Yanhui Su^{a,b,1}, Yong Ma^{a,b}, Le Wei^{a,b}, Ying He^{a,b}, Yuting Gu^{a,b}, Shiwei Mei^{a,b}, Qiaoqiao Mu^{a,b}, ChengYuan Peng^{a,b}, Yang Peng^{a,b}, Zhao Deng^{a,b,*}

^a Soochow Institute for Energy and Materials Innovations, College of Energy, Soochow University, Suzhou 215006, PR China

^b Key Laboratory of Advanced Carbon Materials and Wearable Energy Technologies of Jiangsu Province, Soochow University, Suzhou 215006, PR China

ARTICLE INFO

Keywords:

Li-O₂ battery
Photocathode catalyst
Tris(2,2-bipyridine) cobalt(II)
Lithium peroxide
Electron mediator

ABSTRACT

Photo-assisted charge/discharge has witnessed marked success in Li-O₂ batteries (LOBs) to overcome the sluggish kinetics of triphasic reactions at the cathode, but challenges remain to develop high-efficiency but low-cost photocathode catalysts. Herein, a photoactive electron mediator is applied, for the first time, as bifunctional photocathode catalyst in solar-assisted LOBs. The facilely synthesized tris(2,2-bipyridine) cobalt(II) complex (Co-bpy) manifests good electrocatalytic activity in dark and high photoactivity under illumination, concertedly affording an superior charge/discharge voltage gap of 0.12 V and round-trip efficiency of 97%. Moreover, a significantly enhanced charge/discharge reversibility was attained under illumination and attributed to the light-induced amorphization of Li_2O_2 that further extends the cycle life. A two-circuit model is proposed to rationalize the better reduction of charge/discharge polarization at lower operating current density. This work not only extends the family of photocathode catalysts to small-molecule complexes, but also offers new insights into the mechanism of photoenergy storage in LOBs.

1. Introduction

The ever-growing demand on renewable energy sources and their utilization in a carbon-neutral fashion have put forward the development of efficient energy storage devices in high priority [1–3]. Aprotic Li-O₂ batteries (LOBs) based on the reversible reaction $\text{O}_2 + 2\text{Li}^+ + 2\text{e}^- \leftrightarrow \text{Li}_2\text{O}_2$ ($E^0 = 2.96 \text{ V vs Li/Li}^+$) are one of the promising candidates owing to their high energy density of $\sim 3600 \text{ Wh kg}^{-1}$ and utilization of oxygen in air as the cathode active material [4–6]. Despite the notable advantages, hurdles remain to overcome the sluggish kinetics of the triphasic reaction at the cathode surface and the high energy barrier to decompose the insoluble and insulative discharge product of Li_2O_2 [5]. On one hand, the accumulative deposition of Li_2O_2 at the cathode/electrolyte interface during charge/discharge would inevitably mask the catalyst active sites, blockade the gas and liquid permeation, and ultimately shut off the redox electron transfer [7–10]. On the other hand, the high charging overpotential associated with Li_2O_2 decomposition surpassing the electrochemical window of electrolyte would incur severe parasitic reactions that drastically curtail the battery life [7,11]. Thus, one of the

key tasks in deploying the Li-O₂ technology is to lower the overpotentials for reversible Li_2O_2 formation/decomposition [12], and thereby improve the round-trip energy efficiency and alleviate parasitic side reactions.

Tremendous efforts have been devoted to addressing the above-mentioned issues, including the exploitation of potent electrocatalysts (e.g. Pt/Au [13,14], Ru/RuO₂ [15–17], Co_xO_y [18,19], MnO₂ [6,20–22], NiCo₂O₄ [23] etc.) to lower the activation barrier and regulate the reaction path for Li_2O_2 formation/decomposition, as well as the application of redox mediators (e.g. TTF, FC, InBr, LII [24–26] etc.) to expedite the reaction kinetics through electron relay. Recently, the efficiency of LOBs has been seen improved by further applying various external physical fields [27,28]. Among them, photo-assisted LOBs have attracted most attention in virtue of the dramatic increase in round-trip energy efficiency through the storage of photoenergy into electrochemical energy [5,29,30]. It has been shown that the photovoltaic effect incorporated into LOBs can not only reduce the overpotentials for oxygen reduction and evolution reactions (ORR/OER), but also expedite the Li_2O_2 decomposition and suppress the intermediate-LiO₂ lifetime

* Corresponding author at: Soochow Institute for Energy and Materials Innovations, College of Energy, Soochow University, Suzhou 215006, PR China.

E-mail address: zdeng@suda.edu.cn (Z. Deng).

¹ Contributed equally to this work.

[31–33]. For instance, by fabricating a bifunctional photocathode composed of $\text{TiO}_2\text{-Fe}_2\text{O}_3$ heterojunctions, Xu et al. demonstrated the tailoring of Li_2O_2 morphology to enhance the OER kinetics, resulting in an outstanding low discharge/charge potential gap of 0.19 V [32]. Yang et al. reported a bifunctional CeVO_4 catalyst that not only lowers the charge overpotential to 0.52 V through a photo-assisted mechanism, but also suppresses highly reactive LiO_2 intermediates to avoid the oxidative decomposition of electrolyte and cathode materials during discharge [34]. By electrospinning photoactive and catalytic WSe_2 moieties into CNT-reinforced carbon nanofibers, our group have also shown that upon illumination the Li_2O_2 morphology can be converted from a toroidal morphology in dark to a thin-film coating wrapping around the fibers, leading to significantly lowered polarization and extended capacity [35]. Notwithstanding, it must be noted that all the photoactive materials exemplified above involve relatively complex synthetic measures that are both time and energy-consuming, not to mention the better-desired energy efficiency and cycling stability.

Previous studies have illustrated that an ideal photocatalyst to be employed in solar-assisted LOBs should possess not only good electrocatalytic activity, but also potent photoactivity with suitable band structure to catalyze both the ORR and OER reactions [33,36]. In view of these attributes, metal-organic complexes with catalytically active metal centers such as Co, Ni, Cu, and tunable frontier orbital configuration (and thus tunable band structure) are highly intriguing [37–39]. Chen et al. have shown that semiconducting metal-organic polymer nanosheets composed of cobalt-tetramino-benzoquinone (Co-TABQ) could serve as photocatalyst for enhancing the kinetics of cathode reactions under visible light. They ascribed the ORR reaction to the photo-activated metal-ligand charge transfer (MLCT) and the OER process to photo-vacated d orbitals in the transition metal center [40]. Inspired by this work, in the current study we extend, for the first time, the photocatalyst in solar-assisted LOBs to small-molecule complex. We chose the compound of tris(2,2'-bipyridine) cobalt(II) (Co-bpy) based on the following considerations: 1) the compound can be easily synthesized through a precipitation reaction in atmospheric condition; 2) the Co-N coordination with an O_h symmetry has been reckoned as an efficient catalyst for oxygen conversion reactions [41,42]; 3) the complex is colored in yellow and potentially photoactive; 4) the facile conversion between Co(II)-bpy and Co(III)-bpy allows it to serve as the electron mediator for expediting the redox kinetics [43]. As a result, LOBs employing Co-bpy as the photocathode catalyst achieve an ultralow discharge/charge voltage gap of 0.12 V under illumination, accounting for a round-trip efficiency of 97%, and a long-term cyclability of 60 and 330 cycles under continuous and intermittent illumination, respectively.

2. Experimental section

2.1. Chemicals

2,2'-Bipyridyl and Cobalt chloride hexahydrate were procured from Aladdin (Shanghai) Co., Ltd. Anhydrous ether was purchased from Sinopharm Chemical Reagent Co., Ltd. Anhydrous methanol was purchased from Jiangsu Qiangsheng functional Chemistry Co., Ltd. $\text{TiO}_4\text{-SO}_4\text{-xH}_2\text{SO}_4\text{-xH}_2\text{O}$ (93%) were provided by Aladdin (Shanghai) Co., Ltd. All chemicals were of analytical grade and used as received.

2.2. Sample preparation

The small-molecule compound of tris(2,2'-bipyridine) cobalt(II) was prepared as follow. First, 0.01 mol (2.3793 g) $\text{CoCl}_2\cdot 6\text{H}_2\text{O}$ was added to a 100 mL round bottom flask containing 20 mL methanol. Then, 0.03 mol (4.68552 g) bipyridine was dissolved in 20 mL methanol, and subsequently added dropwise into the above CoCl_2 solution (Fig. S1). Afterwards, the solution was stirred for 2 h at 50 °C. After cooling to room temperature, about 2/3 of the solvent was removed by rotary evaporation, followed by adding 30 mL anhydrous ethyl ether and

standing for 20 min. Finally, the resultant precipitates were filtered out and vacuum-dried at 80 °C for overnight.

2.3. Characterization

Mass spectra were recorded using a Bruker Ultraflextreme MALDI-TOF instrument. Fourier transform infrared spectroscopy (FTIR, Bruker Tensor 27) was used to analyze the functional groups of samples. Raman spectra were acquired using a confocal laser Raman microscopy (Horiba Jobin Yvon, HR Evolution). The sample morphology was examined by field-emission scanning electron microscopy (FE-SEM, Hitachi SU8010). Powder X-ray diffraction (pXRD) spectra were acquired by a Bruker D8 ADVANCE diffractometer equipped with the $\text{Cu-K}\alpha$ radiation source. X-ray photoelectron spectroscopy (XPS, Thermo Fisher, ESCALAB 250Xi) equipped with a monochromated Al $\text{K}\alpha$ source was used to characterize the elemental composition and chemical states of samples. UV-Vis spectra were recorded with a Lambda 750 S spectrometer (PerkinElmer, USA). The photoluminescence (PL) spectra were obtained by a fluorescence spectrometer (HORIBA, Fluoromax-4) with a Xenon lamp (150 W) as the excitation light. Ultraviolet Photoelectron Spectroscopy (UPS) was performed on an Escalab 250Xi system (Thermo Fisher, USA) with the pristine Au used for Fermi level calibration. Photocurrent tests were conducted through a CHI-660D electrochemical workstation (Shanghai Chenhua, China) in a Li-O₂ Battery setup by intermittently switching the irradiation light (420 nm) on and off.

2.4. Electrochemical measurements

To prepare the photocathode, the Co-bpy active material, conductive agent of KB, and polyvinylidene fluoride (PVDF) binder were homogeneously mixed in N-methyl-2-pyrrolidone at a ratio of 60%: 30%: 10%. The resultant slurry was casted onto a carbon paper via the doctor blade method, and vacuum dried at 80 °C for 12 h. The active material mass loading on the cathode was about 0.25 ± 0.05 mg and based on that the specific capacity and current density were calculated. The assembly of 2032-type coin cells was conducted in an Ar-filled glove box with the contents of H_2O and O_2 maintained below 0.1 ppm. In each cell, 1.0 M LiTFSI in Tetraglyme of 160 μL was used as the electrolyte without additional additives, and a glass fiber disk of 19 mm in diameter (Whatman GF/D) was used as the separator. Galvanostatic charge/discharge measurements were carried out on a LAND CT2001A battery testing system in homemade gas-tight testing bottles filled with oxygen (Fig. S2). Electrochemical impedance spectrometry (EIS) measurements were performed using a Zahner Zennium-E electrochemical workstation within the frequency range set from 100k to 0.01 Hz at an amplitude of 5 mV. Cyclic voltammetries (CV) were conducted on a CHI-760E electrochemical workstation with the scan rate set at 0.1 mV s^{-1} . Differential electrochemical mass spectrometry (DEMS) experiments were conducted on a quadrupole mass spectrometer (Prisma Plus QME220) with the gas inlet connected to a customized Swagelok cell assembly.

3. Results and discussion

3.1. Structure and optical properties of Co-bpy

The complex of tris(2,2'-bipyridine) cobalt(II) (abbreviated as Co-bpy) was synthesized by a one-pot reaction as detailed in the experimental section. In this small-molecule compound, each cobalt is coordinated with three bipyridines as witnessed by the mass spectrometry (MS) shown in Fig. 1a. Fourier Transform Infrared Spectrum (FT-IR) taken on Co-bpy showed notable Co-N signals at 418 and 1016 cm^{-1} , corresponding to the asymmetric and symmetric stretching $\nu_{(\text{Co-N})}$ vibration modes, respectively (Fig. 1b) [44–48]. Other peaks associated with the C-H, C=C, and C=N bonding in bpy also underwent wavenumber shift and intensity change after the formation of the Co-bpy complex. Similarly, the Raman spectrum of Co-bpy also manifests

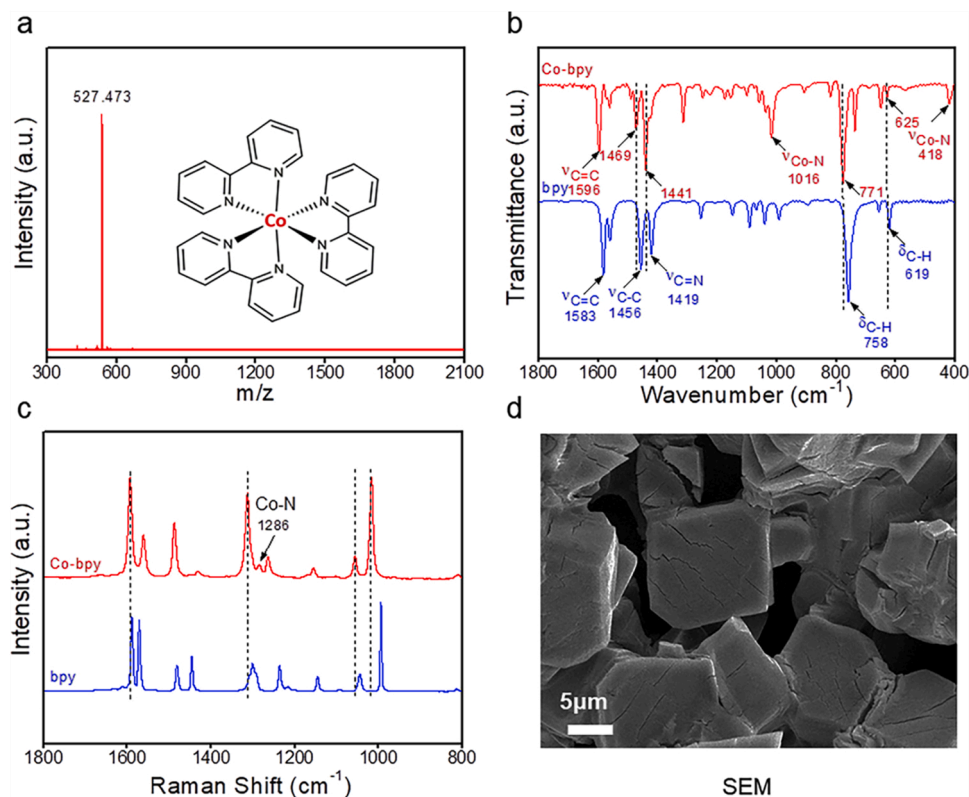


Fig. 1. Structural characterization of Co-bpy. (a) Mass spectrum; the inset image shows the molecule structure of Co-bpy with an O_h coordination symmetry. (b) FT-IR and (c) Raman spectra of Co-bpy in comparison to the bpy ligand. (d) SEM image of the crystallized Co-bpy.

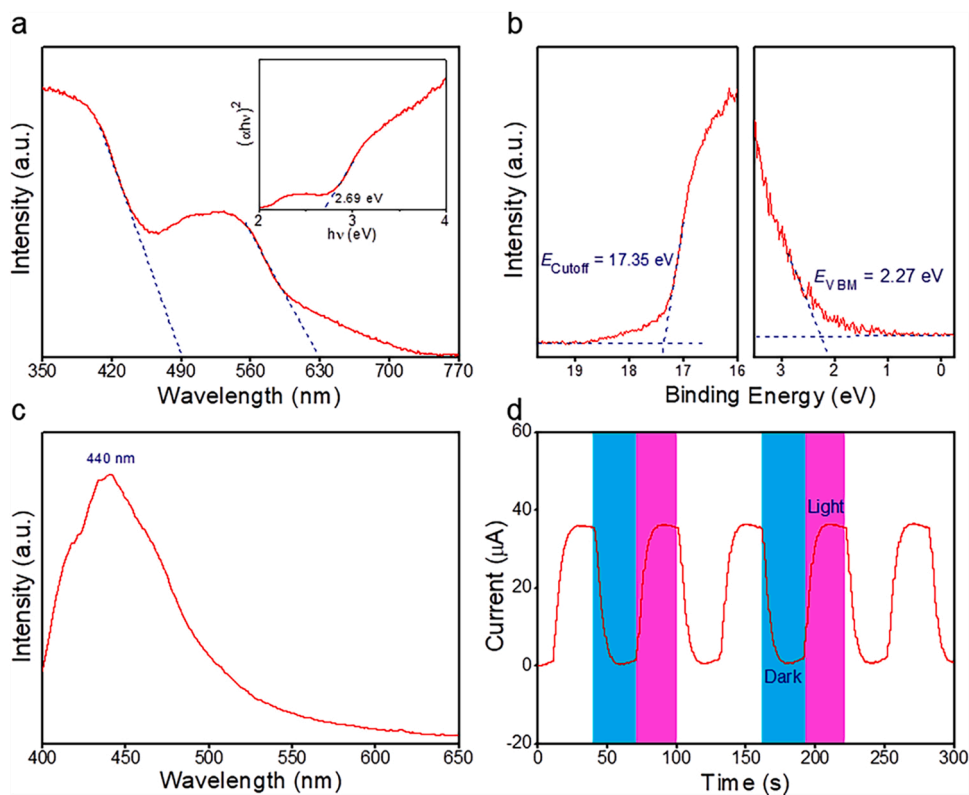


Fig. 2. Optical properties of Co-bpy. (a) UV-Vis DRS spectrum of Co-bpy with the corresponding Tauc plot shown in the inset. (b) UPS spectrum. (c) Steady-state PL spectrum. (d) TPR i-t plot.

quite different vibration pattern to that of bpy due to the metal-ligand coordination (Fig. 1c), which is in good agreement with previous studies [49,50]. The peak at 1286 cm^{-1} attributed to $\nu_{(\text{Co-N})}$ vibration provides a strong evidence for the Co(II) coordination in an octahedral ligand field. Scanning electron microscopy (SEM) image in Fig. 1d shows that the Co-bpy compound is well-crystallized, exhibiting multi-facet exposure.

The optical properties of Co-bpy were characterized by Ultraviolet-Visible Diffuse Reflection Spectroscopy (UV-Vis DRS), Photoluminescence Spectroscopy (PL), Transient Photocurrent Response (TPR) and Ultraviolet Photoelectron Spectroscopy (UPS). The DRS spectrum shown in Fig. 2a reveals a major band with the extrapolated absorption edge from 490 nm and a shoulder with the absorption onset at 750 nm, endorsing the superb light absorption of the complex. The corresponding Tauc plot (Fig. 2a inset) indicates the main absorption at lower wavelength dominates the band structure, manifesting a band gap (E_g) of 2.69 eV. The observed band characteristics of Co-bpy with multiple absorptions of varying intensity can be well understood from the frontier orbital theory in association with the selection rules [51–54]. UPS measurements further reveal that the work function of Co-bpy is 3.87 eV and the valence band maximum (VBM) is situated at 2.27 eV below the Fermi level (Fig. 2b). Therefore, the energy level of VBM is approximated at 6.14 eV (vs. Vacuum) for Co-bpy. This in turn gives a conduction band minimum (CBM) located at 3.45 eV (vs. Vacuum). By translating the vacuum-zeroed energy coordinate to that zeroed by the standard electrochemical potential of Li/Li^+ , we can then further deduce the CBM, VBM, and FE of Co-bpy, respectively positioned at 2.05, 4.74, and 2.47 V vs. Li^+/Li (Fig. S3). Note that the CBM and VBM of Co-bpy span across the standard electrochemical potential of 2.96 V (vs. Li/Li^+) for the reaction $\text{Li} + \text{O}_2 \rightarrow \text{Li}_2\text{O}_2$.

The steady-state PL spectrum of Co-bpy in Fig. 2c shows an emission peak centered at 440 nm under the excitation of 350 nm, further confirming the fact that the main UV-Vis absorption peak with the onset at 490 nm dictates the optical band structure of Co-bpy. By consecutively truncating the light illumination, Co-bpy demonstrated efficient photocurrent response in the TPR spectrum shown in Fig. 2d. The average density of photocurrent reaches to $37.5\text{ }\mu\text{A cm}^{-2}$, in contrast to the near-zero current density in dark, and remains constant during the whole testing period of 300 s. Collectively, all the optical and photochemical characterizations above, in conjunction with the well-reckoned catalytic activity of Co-based complexes [55–57], forecast Co-bpy a potential photocatalysts to be utilized in solar-assisted Li-O₂ batteries.

3.2. Electrocatalytic performance of Co-bpy

The electrochemical properties of Co-bpy as the oxygen-cathode catalyst were assessed in the coin-type LOBs and compared with KB. First of all, the cathode loaded with Co-bpy showed good stability in the tetraglyme electrolyte containing 1.0 M LiTFSI. After soaking for 72 h, there was no color change observed for the electrolyte, indicative of no dissolved Co-bpy (Fig. S4). This was further confirmed by UV-Vis spectra taken on the electrolyte before and after soaking, revealing negligible change of the absorption bands (Fig. S5). To further interrogate the stability of Co-bpy on the electrode under continuous bias, a three-electrode configuration was adopted to repeatedly conduct cyclic voltammetries (CVs) in the aforementioned electrolyte (Fig. S6). UV-Vis spectra taken on the electrolyte extracted after the 3rd and 12th cycle revealed no featured absorption of Co-bpy, corroborating its good electrochemical stability (Fig. S7).

CVs taken on the LOBs of Co-bpy and KB within the potential range of 2.0–4.5 V (vs. Li^+/Li) were given in Fig. S8. For Co-bpy, the cathodic current is peaked at 2.21 V with a maximum of 2.22 mA, whereas the peak cathodic current of KB is located at 2.10 V with a much lower value of 1.12 mA. This observation points to the lower polarization and higher kinetics of the ORR reaction ($\text{O}_2 + 2\text{Li}^+ + 2\text{e}^- \rightarrow \text{Li}_2\text{O}_2$) catalyzed by Co-

bpy. On the anodic scan, the catalytic effect of Co-bpy is even more distinct. Two anodic peaks at 3.53 and 4.05 V can be clearly identified, corresponding to the stepwise decomposition of Li_2O_2 through the OER reactions ($\text{Li}_2\text{O}_2 \rightarrow \text{LiO}_2 + \text{Li}^+ + \text{e}^-$; $\text{LiO}_2 \rightarrow \text{O}_2 + \text{Li}^+ + \text{e}^-$) [9,58,59]. In a stark contrast, there is no obvious anodic peak observed on the CV curve of KB. We thus surmise Co-bpy, as the electron mediator [43,60,61], plays a key role to relay the electron transfer in the reaction cascade through the redox couple $[\text{Co}(\text{bpy})_3]^{2+}/[\text{Co}(\text{bpy})_3]^{3+}$. Since Co-bpy in this case is loaded on the oxygen cathode, it is only involved in half reactions on the cathode, i.e. $\text{O}_2 + \text{Li}^+ + \text{e}^- \leftrightarrow \text{LiO}_2$, $E^0 = 2.65\text{ V}$ (vs. Li^+/Li); $\text{LiO}_2 + \text{Li}^+ + \text{e}^- \leftrightarrow \text{Li}_2\text{O}_2$, $E^0 = 3.27\text{ V}$ (vs. Li^+/Li); $\text{O}_2 + 2\text{Li}^+ + 2\text{e}^- \leftrightarrow \text{Li}_2\text{O}_2$, $E^0 = 2.96\text{ V}$ (vs. Li^+/Li) [62]. As an effective electron mediator, the $[\text{Co}(\text{bpy})_3]^{2+}/[\text{Co}(\text{bpy})_3]^{3+}$ couple ($E^0 = 0.56\text{ V}$ vs. SHE) can readily donate or extract electrons to drive the above reactions [63]. By further comparing the total area of all cathodic and anodic peaks, one can clearly see that Co-bpy produces more discharge products of Li_2O_2 than KB does. Therefore, a good ORR/OER catalytic activity can be expected for Co-bpy when applied as the cathode catalyst in Li-O₂ batteries.

In accordance with the CV measurements, LOBs utilizing Co-bpy as the cathode catalyst demonstrated much improved charge/discharge overpotentials. When charged and discharged at the current density of 100 mA g^{-1} with a cut-off capacity of 1000 mAh g^{-1} , the battery of Co-bpy showed a mid-term charge/discharge potential gap of 0.84 V in the first cycle (Fig. 3a), in contrast to 1.21 V for the KB-based battery (Fig. 3b). After 60 cycles, the terminal charging potential of the Co-bpy cell was still less than 5 V and the mid-term charge/discharge voltage gaps increased to 2.16 V (Fig. 3a). In comparison, the terminal charging potential of the KB cell surpassed 5 V after only 30 cycles with a mid-term charge/discharge voltage gaps of 2.26 V (Fig. 3b). Nonetheless, it is worth to note that the slowly increase of charge/discharge polarization observed on the Co-bpy cell suggests there is still plenty room for improving the charge/discharge reversibility.

To interrogate the discharge/charge reversibility of the Co-bpy cell, in-situ differential electrochemical mass spectrometry (DEMS) was utilized to track the O_2 consumption/evolution and quantify the faradaic efficiencies. During discharge, an obvious decrease in oxygen flux was monitored by MS. Integration of the O_2 consumption against total faradaic current resulted in a e^-/O_2 number of 1.84, which is slightly less than the theoretical value of 2 for Li_2O_2 formation and accounts for a faradaic efficiency of 92% for O_2 conversion (Fig. 3c). It is generally recognized that the formation of Li_2O_2 in the crystalline form involves the solvated intermediate of LiO_2 , which is highly active in reacting with both the electrolyte and electrode materials (including even carbon) [64–66]. Therefore, it is not surprised to see that the DEMS study only gave a e^-/O_2 ratio of 1.84, meaning some oxygen were consumed without giving faradaic current. In the subsequent charging process, the number of e^-/O_2 (evolution) was quantified to be 2.05, apart from the observation of trivial CO_2 due to carbon oxidation and/or electrolyte decomposition (Fig. 3d). Additionally, the total amount of oxygen evolution ($0.61\text{ }\mu\text{mol}$) during charge is lower than that of oxygen consumption ($0.72\text{ }\mu\text{mol}$) during discharge. Together, these results indicate that the discharge and charge processes are not fully reversible and accompanied with side reactions.

Raising the operating current progressively from 100 to 1000 mA g^{-1} in the galvanostatic cycling test, the LOB of Co-bpy further manifested a superior rate capability to that of KB (Fig. 3e). Particularly, in the ten consecutive cycles operated at 1000 mA g^{-1} the electrocatalyst of Co-bpy lent an average discharge voltage of 2.59 V, which is 0.17 V higher than that of KB. Once the operating current was switched back to 100 mA g^{-1} , the discharge voltage of the Co-bpy cell was fully recovered and maintained constant, whereas that of the KB cell deteriorated quickly. More impressively, the LOB of Co-bpy demonstrated an ultrahigh specific capacity of 51650 mAh g^{-1} at 100 mA g^{-1} (taking into account the total weight of Co-bpy and KB on the cathode), doubling that of the KB cell with a total discharge capacity of 25418 mAh g^{-1}

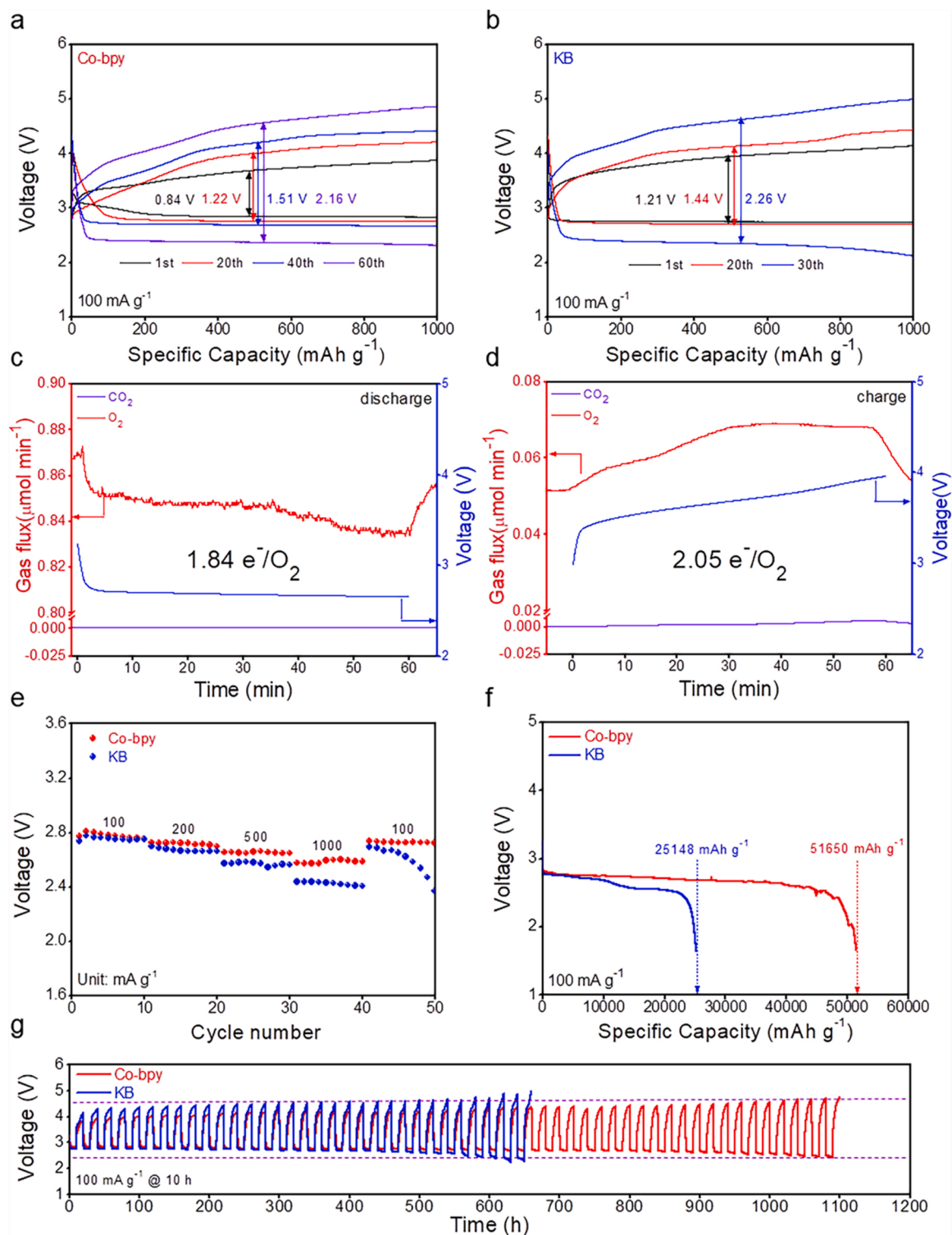


Fig. 3. Electrochemical performance of Co-bpy in Li-O₂ batteries. (a, b) Serial charge and discharge curves taken on the a) Co-bpy and b) KB cells showing the mid-term charge/discharge potential gaps. (c, d) In Situ DEMS spectra taken at the first c) discharge and d) charge of the Co-bpy cell. (e) Rate capability, (f) total discharge capacity and (g) cycling stability measured for Li-O₂ batteries of Co-bpy and KB.

(Fig. 3f). Increasing the charge/discharge current density to 500 mA g⁻¹, a high specific capacity of 21088 mAh g⁻¹ can still be attained, further testifying the great rate performance of Co-bpy (Fig. S9). The cycling stability tests in Fig. 3g show that Co-bpy is capable of maintaining a long cycling stability of 1100 h till the charging voltage hit 4.5 V, in great contrast to the cycling life of 600 h for the KB cell tested under the same condition (1000 mAh g⁻¹ at 100 mA g⁻¹).

Raising the operating current density to 200 and 500 mA g⁻¹, LOBs of Co-bpy can still achieve a stable operation for 716 and 430 h (Fig. S10), respectively, which are much better than the performance of the KB cells. Taken together, the above electrochemical tests unanimously attest to the high efficacy of Co-bpy in catalyzing the Li-O₂ reaction in LOBs, albeit not fully reversible. Apart from Co-bpy, other cobalt-based compounds such as Co-FPOH[38], Co-TABQ[40], Co-C₃N₄[67] and

Co-CTF/KB[68] have been also reported to facilitate O_2 adsorption and catalyze its conversion on the porous cathode, which markedly improve the kinetics of the oxygen conversion reactions.

3.3. Photo-electrochemical performance

In virtue of the afore-demonstrated photoactivity of Co-bpy, the assembled LOBs were further inspected under illuminated conditions. CVs taken on the illuminated Co-bpy cell displayed similar redox features to those observed in dark, with two anodic peaks located at 3.33 and 3.56 V and one large cathodic peak centered at 2.33 V (Fig. S11). Note that both the anodic/cathodic voltage gap and current density under illumination were significantly improved when compared to those observed in dark (Fig. S8), implying that the cell polarization can be mitigated through light irradiation. In addition, the null CV curve in Ar confirms that the redox peaks observed above were indeed from oxygen reactions. Fig. 4a compares the first discharge/charge curves of LOB at 100 mA g^{-1} with and without illumination. Strikingly, the terminal discharge voltage under illumination raised to 3.45 V from the value of 2.85 V in dark, even exceeding the thermodynamic equilibrium potential of 2.96 V (vs. Li^+/Li). Meanwhile, the terminal charge potential

under illumination decreases to 3.57 V, leading to an ultralow charge/discharge potential gap of 0.12 V and an extraordinary round-trip efficiency of 97%. Thus, it becomes obvious that the charge/discharge polarization of LOB can be effectively compensated by the photovoltaic effect of Co-bpy.

The outstanding LOB performance under illumination can be preserved for at least 60 cycles (Fig. 4b), after which the Xeon lamp had to be shut off to avoid overheating. At the current density of 500 mA g^{-1} , the LOB of Co-bpy under illumination demonstrated both enhanced capacity (Fig. S12, S13) and cycling behavior (Fig. S14), but the contrast between light and dark conditions was less stark when compared to the low-current scenario shown in Fig. 4a and b. This phenomenon has been often seen in literature studies and can be attributed to the inadequate photogenerated carriers in comparison to the overall circulating current, which is further witnessed by the rate performance tests with the current density ramped from 100 to 2000 mA g^{-1} (Fig. 4c, with a cycling cut-off capacity of 500 mAh g^{-1}) and will be discussed in more details later. Notwithstanding, at all current densities the LOB under illumination exhibited notable reduction of charge/discharge polarization, which justifies the benefit brought by the photovoltaic effect of Co-bpy.

Electrochemical impedance spectra (EIS) were taken at different

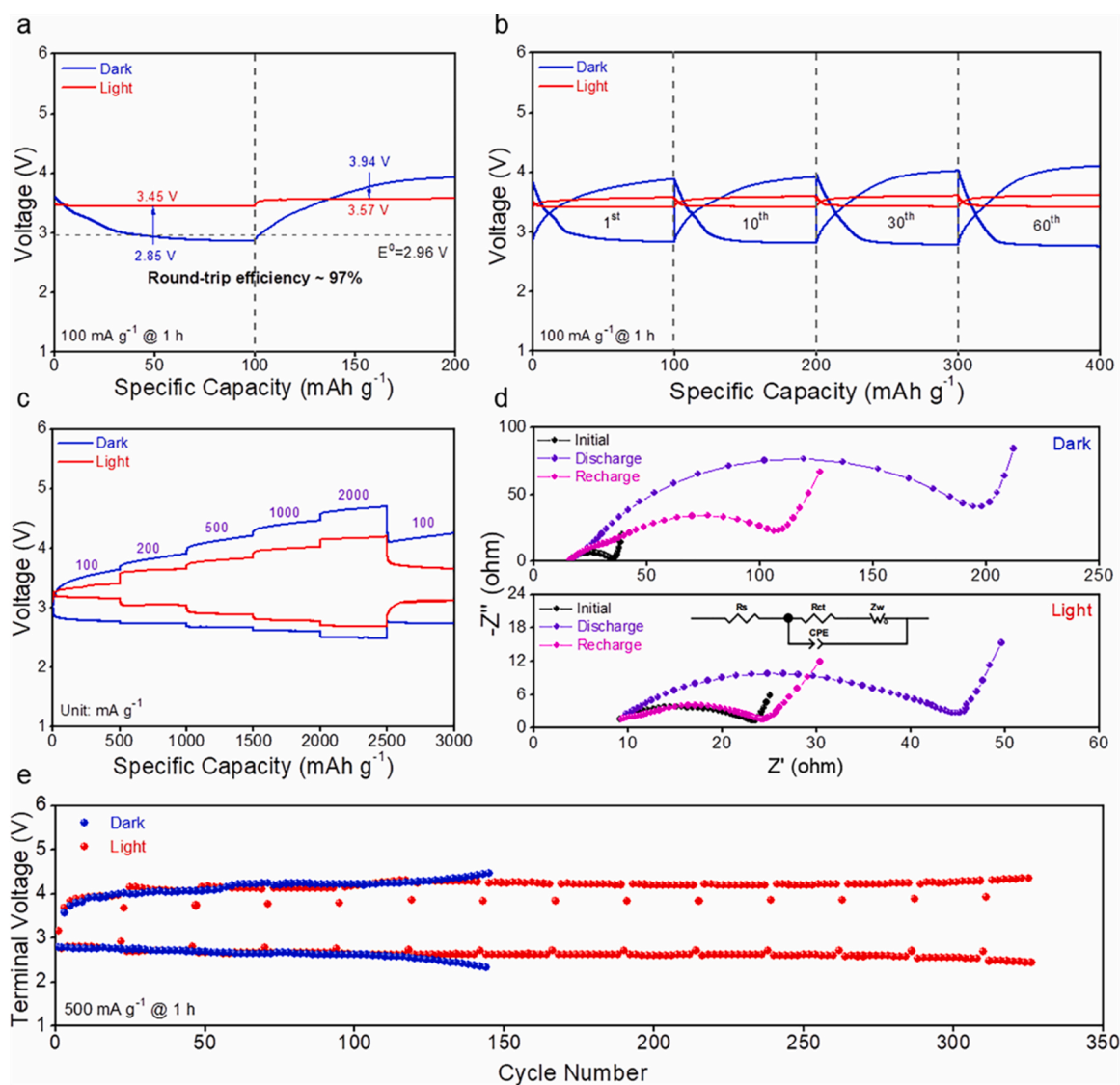


Fig. 4. LOB performance of Co-bpy with and without illumination. (a) First discharge and charge profiles and (b) cycle performance at 100 mA g^{-1} with a cut-off capacity of 100 mAh g^{-1} . (c) Rate performance from 100 to 2000 mA g^{-1} . (d) Nyquist plots taken at different charge/discharge states. (e) Cycling stability under intermittent lighting vs. in dark at 500 mA g^{-1} .

charge/discharge states to interrogate the charge kinetics in LOBs of Co-bpy under dark and illuminated conditions. The Nyquist plots in the top panel of Fig. 4d show that the charge transfer resistance (R_{ct}) after discharge in dark was drastically increased to 155.9 Ω from 22.8 Ω of the initial state, as a result of the formation of insulative Li_2O_2 . After recharging, R_{ct} reduced to 81.2 Ω , suggesting the incomplete decomposition of Li_2O_2 . In a stark contrast, the illuminated LOB showed a much smaller resistance in all charge/discharge states. Specifically, R_{ct} increased from the initial 21.8 Ω to 42.7 Ω of the discharged state, and then returned to 22.3 Ω after recharging. The nearly identical R_{ct} values between the initial and recharged states strongly suggest that light illumination helps to promote reversible Li_2O_2 formation/decomposition. This leads us to further leverage such advantage (of photo-enhanced Li-O₂ reaction reversibility) to remedy the oxygen cathode through intermittent light irradiation for extending the LOB cycle life. As shown in Fig. 4e, by intermittently illuminating the LOB of Co-bpy once per ten cycles, the cycling life can be greatly extended from 145 to 327 cycles at 500 mA g⁻¹, which can be attributed to the photoexcited holes in facilitating the oxidative decomposition of Li_2O_2 , rendering a cleaner electrode surface with mitigated Li_2O_2 accumulation. This argument was further supported by a parallel test designed to compare the contributions from illuminated discharge or charge to the cycling behaviors, revealing much alleviated charge/discharge polarization with the application of only lighted charging (Fig. S15).

3.4. Mechanistic insights into the reversible Li_2O_2 formation/decomposition under illumination

It is known that suitable energy levels of CB and VB are key to the photocatalysts in catalyzing reversible ORR and OER reactions in photo-assisted Li-O₂ batteries [8,33,69]. Scheme 1 illustrates the energy band diagram for the LOB of Co-bpy assessed in this study. As aforementioned, Co-bpy possesses conduction and valence bands respectively positioned at 2.05 and 4.74 V (vs. Li^+/Li), spanning across the equilibrium potential of $\text{Li}/\text{Li}_2\text{O}_2$ (2.96 V vs. Li^+/Li). Upon illumination, photoelectrons are excited to the conduction band, leaving an identical number of holes in the valence band. During discharging, the photoelectrons are consumed to reduce O_2 to form Li_2O_2 and Li_2O_2 by reacting with Li^+ traversed from the anode. The outcome is the rise of the discharge voltage from its equilibrium potential as driven by the photovoltage, meaning the conversion of photoenergy to electricity. On the other hand, during charging the decomposition of Li_2O_2 is facilitated by the holes in the valence band, which helps to lower the OER overpotential. Meanwhile, the photoelectrons are propelled to reduce Li^+ at anode via the external circuit.

As the photogenerated carriers are typically limited to some extent, the photovoltaic effect becomes more eminent at lower operating

current. This can be well understood from the two different electron transfer paths (namely the electrochemical path I and photoexcited path II) in contributing to the total external current shown in Scheme 1. Taking the discharge process as an example, energy conservation requires:

$$V_{\text{dis}}I_{\text{dis}} = I_1 \times V_{\text{eq}} + I_2 \times V_{\text{VB}} - \text{OP} \times I_{\text{dis}} \quad (1)$$

$$I_{\text{dis}} = I_1 + I_2 \quad (2)$$

$$\text{Thus, } V_{\text{dis}} = I_1/I_{\text{dis}} \times V_{\text{eq}} + I_2/I_{\text{dis}} \times V_{\text{VB}} - \text{OP} \quad (3)$$

$$\text{Make } n_1 = I_1/I_{\text{dis}}; n_2 = I_2/I_{\text{dis}}$$

$$\text{We get } V_{\text{dis}} = n_1 \times V_{\text{eq}} + n_2 \times V_{\text{VB}} - \text{OP} \quad (4)$$

Where I_1 is the portion of external circuit current associated with the reduction of O_2 to Li_2O_2 (note that part of O_2 is also reduced by the photoelectrons from CB), I_2 is the other portion of external circuit current associated with the neutralization of photogenerated holes on VB, OP is the discharge overpotential.

Consequently, the discharge voltage can be represented by a linear combination of V_{eq} and V_{VB} minus the overpotential. When the total discharge current is small, the path II of electron transfer dictates due to the higher driving potential, and thus one should see a significant rising of discharge voltage. As the operating current increases, Path I takes a larger cut of the pie (due to the inadequate photocarriers) and ultimately overwhelms Path II. Similarly, Eqs. 5–7 illustrate the relation among V_{cha} , V_{eq} , V_{CB} and OP in the charging process, where Path II also takes a priority to Path I due to the lower needed work.

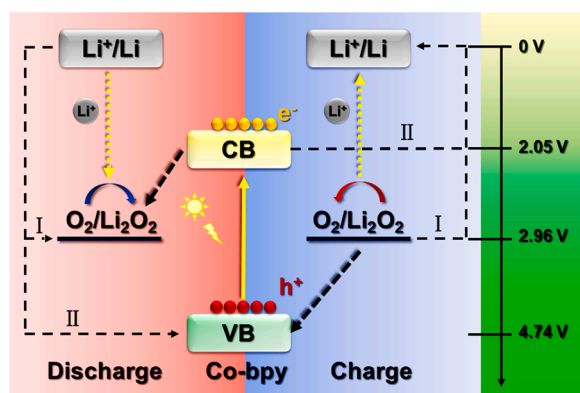
$$V_{\text{cha}}I_{\text{cha}} = I_1 \times V_{\text{eq}} + I_2 \times V_{\text{CB}} + \text{OP} \times I_{\text{cha}} \quad (5)$$

$$I_{\text{cha}} = I_1 + I_2; n_1 = I_1/I_{\text{cha}}; n_2 = I_2/I_{\text{cha}} \quad (6)$$

$$V_{\text{cha}} = n_1 \times V_{\text{eq}} + n_2 \times V_{\text{CB}} + \text{OP} \quad (7)$$

Collectively, the above discussions should help rationalize the drastically reduced discharge/charge voltage gap at low rates. However, it should be noted that even at very low current densities the charge and discharge overpotentials caused by electrode polarization, ohmic contact and interfacial resistance are insurmountable, which should help to comprehend the difference between the measured discharge/charge voltages and their theoretical values.

To characterize the Li_2O_2 morphology on Co-bpy cathodes with and without illumination, SEM images were taken. As shown in Fig. 5a, the illuminated cathode presents a thick and uniform layer of lamellar Li_2O_2 products, which are mostly disappeared after charging (Fig. 5b). XRD detected no signals belong to crystalline Li_2O_2 (Fig. 5c), suggesting the amorphous nature of the discharge products. In addition, the cathode morphology after illuminated charging almost completely recovered to its initial state (Fig. 5b vs. S16), affirming the high reversibility of Li_2O_2 formation/decomposition under illumination. Previous studies have attributed the amorphous thin-film like Li_2O_2 products to a surface growth mechanism that is facilitated by enhanced charge transfer kinetics [1,70,71]. Here, Co-bpy, serving as the efficient oxygen catalyst and electron mediator, helps to effectively relay the electron transfer and further support the surface growth mechanism of Li_2O_2 . In a stark contrast, the morphology of Li_2O_2 formed in dark exhibits the classic toroidal shape (Fig. 5d), ascribed to a solvation-mediated pathway that is thermodynamically driven. After recharging, a significant portion of the discharge products was decomposed, but some toroidal Li_2O_2 particles can be still visualized (Fig. 5e). XRD taken on the cathode discharged in dark further revealed distinct peaks at 32.7° and 34.8°, corresponding to the (110) and (100) planes of Li_2O_2 (JCPDS # 74-0115), respectively. The intensity of all these peaks was notably weakened after charging in dark (Fig. 5f). It is worth to note that there have been controversies in literature over the role of the amorphous thin-film Li_2O_2 products in trading the capacity with rate capability and



Scheme 1. Energy diagram of Co-bpy in reference to Li^+/Li and $\text{O}_2/\text{Li}_2\text{O}_2$ to illustrate the two-circuit model for photo-assisted Li-O₂ battery comprising the electrochemical path I and photoexcited path II.

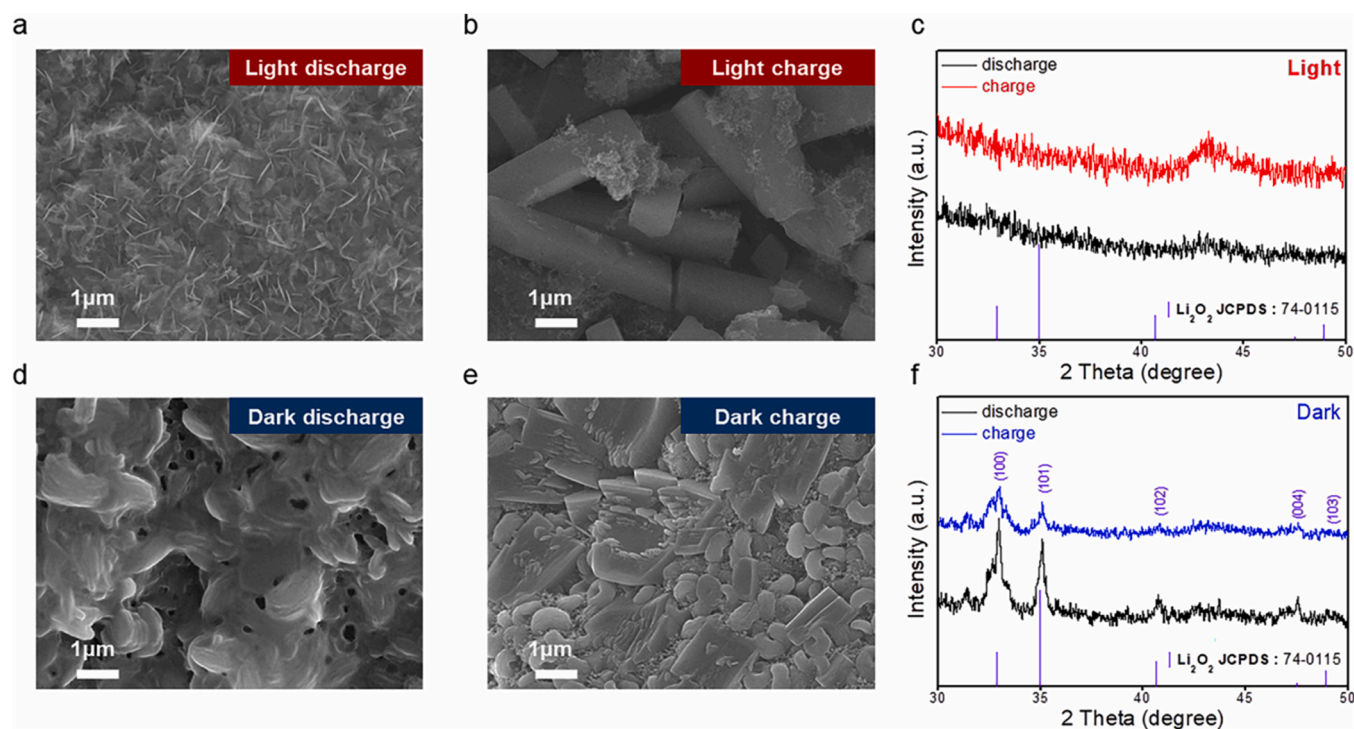


Fig. 5. Post-mortem characterizations on the oxygen cathodes evidencing the reversible Li_2O_2 formation/decomposition under illumination. (a, b) SEM images and (c) XRD patterns taken on the discharged and recharged Co-bpy cathodes under illumination. (d, e) SEM images and (f) XRD patterns taken on the discharged and recharged Co-bpy cathodes without illumination.

reversibility [5,9,72–75]. In our study, as shown in Fig. 5a, the lamellar Li_2O_2 products were grown on the catalyst surface both laterally and vertically, lending plenty voids to allow the permeation of electrolyte and Li^+ . Additionally, the amorphous Li_2O_2 thin film itself might serve as the SEI, allowing Li^+ to penetrate and react with O_2 on the other side of the thin film, leading to both the enhanced capacity and reversibility.

To further confirm that the amorphous thin film formed under illumination is indeed Li_2O_2 , chromometric and DEMS characterizations were carried out. First, to quantitatively compare the Li_2O_2 formation on different cathodes including KB, Co-bpy in dark and Co-bpy under illumination, we discharged all the LOBs with the same capacity of 2 mAh and then immersed the electrodes in 2% aqueous TiOSO_4 solutions. The presence of peroxide (O_2^{2-}) species would turn the solution into a yellow color through the formation of TiO_2^{2+} [76–79]. Hence, the amount of Li_2O_2 formed or left on the cathodes after discharge/charge can be analyzed through UV-Vis spectra (Fig. S17). It can be seen that the quantity of Li_2O_2 formed on the cathode after discharge follows the order: KB < Co-bpy in dark < Co-bpy under illumination, which is consistent with the trend of observed capacity. More impressively, the electrode of Co-bpy after illuminated charge caused only a negligible color change of the TiOSO_4 solution, which strongly testifies the enhanced Li_2O_2 reversibility, which was further supported by the DEMS results (Fig. S18). As our DEMS setup was not able to integrate light illumination, we managed to discharge the cell of Co-bpy under illumination and then run the DEMS analysis by charging the cell in dark. Despite not ideal, this should still help us discern whether or not the amorphous Li_2O_2 products formed under illumination is more facile to decompose without causing severe side reactions. A nearly perfect e^-/O_2 ratio of 2.01 was obtained here, offering collateral evidence for the discharge product of Li_2O_2 , as well as the enhanced reversibility on the illuminated Co-bpy electrode.

Lastly, XPS was employed to characterize the Li 1s state after discharge and recharge on Co-bpy cathodes with and without illumination. When operated in dark, the discharged cathode displayed a prominent Li 1s peak at 55.0 eV, which faded significantly after

recharging (Fig. S19). Similar Li 1s peak was also observed on the illuminated Co-bpy cathode after discharge, but completely disappeared upon recharging (Fig. S20). Taken together, all the comprehensive characterizations above, in conjunction with previous EIS measurements, unequivocally attest to the fact that the reversibility of Li_2O_2 formation/decomposition catalyzed by Co-bpy can be further boosted by light irradiation.

4. Conclusion

In the current study, photoactive small-molecule complex is applied for the first time, to our best knowledge, as a bifunctional photocathode catalyst in solar-assisted Li- O_2 batteries. In dark conditions, the Co-bpy complex with octahedral Co-N coordination manifested a good electrocatalytic activity in lowering the charge/discharge polarization, promoting the redox kinetics, and extending the specific capacity. Under illumination, the charge/discharge voltage gap was further reduced to 0.12 V at 100 mA g^{-1} , accounting for an impressive round-trip efficiency of 97%, which is among the best seen in literature. The reduction in charge/discharge polarization through the introduction of photovoltaics was found more eminent at low operating current density, which was understood by a two-circuit model newly proposed. More importantly, a significantly enhanced charge/discharge reversibility was achieved under illumination and attributed to the light-induced amorphization of Li_2O_2 , which decomposes more easily and helps to further extend the cycling life of the LOBs. By extending the photocathode catalyst to small-molecule electron mediator of high efficiency but low cost and furnishing new insights into the associated charge transport, this work advances materials development and mechanistic understanding for photo-assisted LOBs.

CRediT authorship contribution statement

XinjianLi: Carried out laboratory work of material characterization and electrochemical characterizations, wrote draft of the manuscript.

Yanhui Su: Carried out optical characterization and some of the photoelectrochemical measurements. **Yong Ma and Le Wei:** Gave some constructive suggestions on the experiment. **Ying He and Yuting Gu:** Battery tests and data interpretation. **Shiwei Mei:** SEM data collection. **Qiaoqiao Mu:** Synthesis of materials. **ChengYuan Peng:** XRD data acquisition. **Yang Peng:** Idea initiation, data curation and proofreading. The corresponding author **Zhao Deng:** Initiated and oversaw the project, manuscript proof.

Declaration of Competing Interest

The authors declare that they have no known competing financial interests or personal relationships that could have appeared to influence the work reported in this paper.

Data Availability

Data will be made available on request.

Acknowledgments

This work was financially supported by National Natural Science Foundation of China (No. 22075193, 22072101), Natural Science Foundation of Jiangsu Province (No. BK20211306), the Key Technology Initiative of Suzhou Municipal Science and Technology Bureau (SYG201934), Six Talent Peaks Project in Jiangsu Province (No. TD-XCL-006) and Priority Academic Program Development (PAPD) of Jiangsu Higher Education Institutions.

Appendix A. Supporting information

Supplementary data associated with this article can be found in the online version at [doi:10.1016/j.apcatb.2023.122964](https://doi.org/10.1016/j.apcatb.2023.122964).

References

- W.J. Kwak, Rosy, D. Sharon, C. Xia, H. Kim, L.R. Johnson, P.G. Bruce, L.F. Nazar, Y. K. Sun, A.A. Frimer, M. Noked, S.A. Freunberger, D. Aurbach, Lithium-oxygen batteries and related systems: potential, status, and future, *Chem. Rev.* 120 (2020) 6626–6683, <https://doi.org/10.1021/acs.chemrev.9b00609>.
- Y. Li, J. Lu, Metal-air batteries: will they be the future electrochemical energy storage device of choice? *ACS Energy Lett.* 2 (2017) 1370–1377, <https://doi.org/10.1021/acsenenergylett.7b00119>.
- N. Imanishi, O. Yamamoto, Rechargeable lithium-air batteries: characteristics and prospects, *Mater. Today* 17 (2014) 24–30, <https://doi.org/10.1016/j.mattod.2013.12.004>.
- D. Aurbach, B.D. McCloskey, L.F. Nazar, P.G. Bruce, Advances in understanding mechanisms underpinning lithium-air batteries, *Nat. Energy* 1 (2016) 1–11, <https://doi.org/10.1038/nenergy.2016.128>.
- C. Shu, J. Wang, J. Long, H.K. Liu, S.X. Dou, Understanding the reaction chemistry during charging in aprotic lithium-oxygen batteries: existing problems and solutions, *Adv. Mater.* 31 (2019), 1804587, <https://doi.org/10.1002/adma.201804587>.
- X. Cao, X. Zheng, Z. Sun, C. Jin, J. Tian, S. Sun, R. Yang, Oxygen defect-ridden molybdenum oxide-coated carbon catalysts for Li-O₂ battery cathodes, *Appl. Catal. B: Environ.* 253 (2019) 317–322, <https://doi.org/10.1016/j.apcatb.2019.04.077>.
- J. Lu, L. Li, J.B. Park, Y.K. Sun, F. Wu, K. Amine, Aprotic and aqueous Li-O₂ batteries, *Chem. Rev.* 114 (2014) 5611–5640, <https://doi.org/10.1021/cr400573b>.
- H. Liang, L. Jia, F. Chen, S. Jing, P. Tsiakaras, A novel efficient electrocatalyst for oxygen reduction and oxygen evolution reaction in Li-O₂ batteries: Co/CoSe embedded N, Se co-doped carbon, *Appl. Catal. B: Environ.* 317 (2022), 121698, <https://doi.org/10.1016/j.apcatb.2022.121698>.
- Z. Ma, X. Yuan, L. Li, Z.-F. Ma, D.P. Wilkinson, L. Zhang, J. Zhang, A review of cathode materials and structures for rechargeable lithium-air batteries, *Energy Environ. Sci.* 8 (2015) 2144–2198, <https://doi.org/10.1039/C5EE00838G>.
- V. Viswanathan, K.S. Thygesen, J.S. Hummelshøj, J.K. Nørskov, G. Girishkumar, B. D. McCloskey, A.C. Luntz, Electrical conductivity in Li₂O₂ and its role in determining capacity limitations in non-aqueous Li-O₂ batteries, *J. Chem. Phys.* 135 (2011), 214704, <https://doi.org/10.1063/1.3663385>.
- S. Hyun, B. Son, H. Kim, J. Sanetuntikul, S. Shanmugam, The synergistic effect of nickel cobalt sulfide nanoflakes and sulfur-doped porous carbonaceous nanostructure as bifunctional electrocatalyst for enhanced rechargeable Li-O₂ batteries, *Appl. Catal. B: Environ.* 263 (2020), 118283, <https://doi.org/10.1016/j.apcatb.2019.118283>.
- Y. Ding, Y. Li, M. Wu, H. Zhao, Q. Li, Z.-S. Wu, Recent advances and future perspectives of two-dimensional materials for rechargeable Li-O₂ batteries, *Energy Storage Mater.* 31 (2020) 470–491, <https://doi.org/10.1016/j.ensm.2020.07.041>.
- G. Wang, F. Tu, J. Xie, G. Du, S. Zhang, G. Cao, X. Zhao, High-performance Li-O₂ batteries with controlled Li₂O₂ growth in graphene/Au-nanoparticles/Au-nanosheets sandwich, *Adv. Sci.* 3 (2016) 1500339, <https://doi.org/10.1002/advs.201500339>.
- Y. Zhou, Q. Gu, K. Yin, Y. Li, L. Tao, H. Tan, Y. Yang, S. Guo, Engineering eg orbital occupancy of Pt with Au alloying enables reversible Li-O₂ batteries, *Angew. Chem. Int. Ed. Engl.* 61 (2022), 202201416, <https://doi.org/10.1002/anie.202201416>.
- E. Yilmaz, C. Yogi, K. Yamanaka, T. Ohta, H.R. Byon, Promoting formation of noncrystalline Li₂O₂ in the Li-O₂ battery with RuO₂ nanoparticles, *Nano Lett.* 13 (2013) 4679–4684, <https://doi.org/10.1021/nl4020952>.
- Z. Jian, P. Liu, F. Li, P. He, X. Guo, M. Chen, H. Zhou, Core-shell-structured CNT@RuO₂ composite as a high-performance cathode catalyst for rechargeable Li-O₂ batteries, *Angew. Chem. Int. Ed. Engl.* 53 (2014) 442–446, <https://doi.org/10.1002/ange.201307976>.
- L. Wei, Y. Ma, Y. Gu, X. Yuan, Y. He, X. Li, L. Zhao, Y. Peng, Z. Deng, Ru-embedded highly porous carbon nanocubes derived from metal-organic frameworks for catalyzing reversible Li₂O₂ formation, *ACS Appl. Mater. Interfaces* 13 (2021) 28295–28303, <https://doi.org/10.1021/acsaami.1c06572>.
- W.H. Ryu, T.H. Yoon, S.H. Song, S. Jeon, Y.J. Park, I.D. Kim, Bifunctional composite catalysts using Co₃O₄ nanofibers immobilized on nonoxidized graphene nanoflakes for high-capacity and long-cycle Li-O₂ batteries, *Nano Lett.* 13 (2013) 4190–4197, <https://doi.org/10.1021/nl401868q>.
- Y. Zheng, R. Gao, L. Zheng, L. Sun, Z. Hu, X. Liu, Ultrathin Co₃O₄ nanosheets with edge-enriched {111} planes as efficient catalysts for lithium-oxygen batteries, *ACS Catal.* 9 (2019) 3773–3782, <https://doi.org/10.1021/acscatal.8b05182>.
- A. Debart, A.J. Paterson, J. Bao, P.G. Bruce, Alpha-MnO₂ nanowires: a catalyst for the O₂ electrode in rechargeable lithium batteries, *Angew. Chem. Int. Ed. Engl.* 47 (2008) 4521–4524, <https://doi.org/10.1002/anie.200705648>.
- C. Tang, P. Sun, J. Xie, Z. Tang, Z. Yang, Z. Dong, G. Cao, S. Zhang, P.V. Braun, X. Zhao, Two-dimensional IrO₂/MnO₂ enabling conformal growth of amorphous Li₂O₂ for high-performance Li-O₂ batteries, *Energy Storage Mater.* 9 (2017) 206–213, <https://doi.org/10.1016/j.ensm.2017.07.016>.
- H. Wang, Y. Yang, Y. Liang, G. Zheng, Y. Li, Y. Cui, H. Dai, Rechargeable Li-O₂ batteries with a covalently coupled MnCo₂O₄-graphene hybrid as an oxygen cathode catalyst, *Energy Environ. Sci.* 5 (2012) 7931–7935, <https://doi.org/10.1039/C2EE21746E>.
- L. Wang, T. Zhu, Z. Lyu, J. Zhang, L. Gong, S. Xiao, J. Liu, W. Dong, X. Cui, G. W. Ho, W. Chen, Facile synthesis of flower-like hierarchical NiCo₂O₄ microspheres as high-performance cathode materials for Li-O₂ batteries, *RSC Adv.* 6 (2016) 98867–98873, <https://doi.org/10.1039/C6RA21414B>.
- F. Li, J. Chen, Mechanistic evolution of aprotic lithium-oxygen batteries, *Adv. Energy Mater.* 7 (2017), 1602934, <https://doi.org/10.1002/aenm.201602934>.
- C. Zhang, N. Dandu, S. Rastegar, S.N. Misal, Z. Hemmat, A.T. Ngo, L.A. Curtiss, A. Salehi-Khojin, A comparative study of redox mediators for improved performance of Li-oxygen batteries, *Adv. Energy Mater.* 10 (2020), 2000201, <https://doi.org/10.1002/aenm.202000201>.
- W. Liu, Y. Yang, X. Hu, Q. Zhang, C. Wang, J. Wei, Z. Xie, Z. Zhou, Light-assisted Li-O₂ batteries with lowered bias voltages by redox mediators, *Small* 18 (2022), 2200334, <https://doi.org/10.1002/smll.202200334>.
- X.X. Wang, D.H. Guan, F. Li, M.L. Li, L.J. Zheng, J.J. Xu, Magnetic and optical field multi-assisted Li-O₂ batteries with ultrahigh energy efficiency and cycle stability, *Adv. Mater.* 34 (2022), 2104792, <https://doi.org/10.1002/adma.202104792>.
- P. Tan, X. Xiao, Y. Dai, C. Cheng, M. Ni, Photo-assisted non-aqueous lithium-oxygen batteries: progress and prospects, *Renew. Sustain. Energy Rev.* 127 (2020), 109877, <https://doi.org/10.1016/j.rser.2020.109877>.
- D. Du, Z. Zhu, K.Y. Chan, F. Li, J. Chen, Photoelectrochemistry of oxygen in rechargeable Li-O₂ batteries, *Chem. Soc. Rev.* 51 (2022) 1846–1860, <https://doi.org/10.1039/D1CS00877C>.
- E. Grabowska, Selected perovskite oxides: characterization, preparation and photocatalytic properties-a review, *Appl. Catal. B: Environ.* 186 (2016) 97–126, <https://doi.org/10.1016/j.apcatb.2015.12.035>.
- T.S. Andrade, M.C. Pereira, P. Lianos, High voltage gain in photo-assisted charging of a metal-air battery, *J. Electroanal. Chem.* 878 (2020) 114559, <https://doi.org/10.1016/j.jelechem.2020.114559>.
- M. Li, X. Wang, F. Li, L. Zheng, J. Xu, J. Yu, A. Bifunctional Photo-Assisted Li-O₂ Battery based on a hierarchical heterostructured cathode, *Adv. Mater.* 32 (2020), 1907098, <https://doi.org/10.1002/adma.201907098>.
- N. Yan, X. Gao, Photo-assisted rechargeable metal batteries for energy conversion and storage, *Energy Environ. Mater.* 5 (2021) 439–451, <https://doi.org/10.1002/eeem.2.12182>.
- D. Li, X. Lang, Y. Guo, Y. Wang, Y. Wang, H. Shi, S. Wu, W. Wang, Q.-H. Yang, A photo-assisted electrocatalyst coupled with superoxide suppression for high performance Li-O₂ batteries, *Nano Energy* 85 (2021), 105966, <https://doi.org/10.1016/j.nanoen.2021.105966>.
- L. Wei, Y. Su, Y. Ma, Y. Gu, Y. Qin, X. Wu, Y. He, X. Li, Y. Peng, Z. Deng, Photoluminescent WSe₂ nanofibers as freestanding cathode for Solar-assisted Li-O₂ battery with ultrahigh capacity and transparent casing, *Chem. Eng. J.* 448 (2022), 137591, <https://doi.org/10.1016/j.cej.2022.137591>.
- Z. Zhu, X. Shi, G. Fan, F. Li, J. Chen, Photo-energy conversion and storage in an aprotic Li-O₂ battery, *Angew. Chem. Int. Ed. Engl.* 131 (2019) 19021–19026, <https://doi.org/10.1002/anie.201911228>.
- O.Z. Esezobor, W. Zeng, L. Niederegger, M. Grubel, C.R. Hess, Co-Mabi flies solo: light-driven markovnikov-selective C- and N-alkylation of indoles and indazoles

- without a cocatalyst, *J. Am. Chem. Soc.* 144 (2022) 2994–3004, <https://doi.org/10.1021/jacs.1c10930>.
- [38] L. Song, T. Zheng, L. Zheng, B. Lu, H. Chen, Q. He, W. Zheng, Y. Hou, J. Lian, Y. Wu, J. Chen, Z. Ye, J. Lu, Cobalt-doped basic iron phosphate as bifunctional electrocatalyst for long-life and high-power-density rechargeable zinc-air batteries, *Appl. Catal. B: Environ.* 300 (2022), <https://doi.org/10.1016/j.apcatb.2021.120712>.
- [39] H. Wang, B. Fan, Z. Luo, Q. Wu, X. Zhou, F. Wang, A unique hierarchical structure: NiCo₂O₄ nanowire decorated NiO nanosheets as a carbon-free cathode for Li-O₂ battery, *Catal. Sci. Technol.* 11 (2021) 7632–7639, <https://doi.org/10.1039/D1CY01487K>.
- [40] Q. Lv, Z. Zhu, S. Zhao, L. Wang, Q. Zhao, F. Li, L.A. Archer, J. Chen, Semiconducting metal-organic polymer nanosheets for a photoinvolvement Li-O₂ battery under visible light, *J. Am. Chem. Soc.* 143 (2021) 1941–1947, <https://doi.org/10.1021/acscatal.0c04020>.
- [41] Y. Su, Z. Song, W. Zhu, Q. Mu, X. Yuan, Y. Lian, H. Cheng, Z. Deng, M. Chen, W. Yin, Y. Peng, Visible-light photocatalytic CO₂ reduction using metal-organic framework derived Ni(OH)₂ nanocages: a synergy from multiple light reflection, static charge transfer, and oxygen vacancies, *ACS Catal.* 11 (2020) 345–354, <https://doi.org/10.1021/acscatal.0c04020>.
- [42] Z. Zhang, J. Bao, C. He, Y. Chen, J. Wei, Z. Zhou, Hierarchical carbon-nitrogen architectures with both mesopores and macrochannels as excellent cathodes for rechargeable Li-O₂ batteries, *Adv. Funct. Mater.* 24 (2014) 6826–6833, <https://doi.org/10.1002/adfm.201401581>.
- [43] J. Lin, Y. Hou, Y. Zheng, X. Wang, Integration of [(Co(bpy)₃)₃]²⁺ electron mediator with heterogeneous photocatalysts for CO₂ conversion, *Chem. Asian J.* 9 (2014) 2468–2474, <https://doi.org/10.1002/asia.201402303>.
- [44] C. Chen, W. Bai, Synthesis and characterization of cobalt complex with 2,2'-bipyridyl, *Sichuan Chem.* 20 (2017) 1–3, doi.org/CNKI:SUN:SHYF.0.2017-04-001.
- [45] Y. Deng, L. Li, Synthesis, crystal structure and property of a novel cobalt complex based on 2,2'-bipyridyl, *Guangdong Chem. Ind.* 44 (2017) 70–71, <https://doi.org/10.3969/j.issn.1007-1865.2017.06.030>.
- [46] C. Zhang, J. Yang, K. Hara, R. Ishii, H. Zhang, T. Itoi, Y. Izumi, Anchoring and reactivation of single-site Co-porphyrin over TiO₂ for the efficient photocatalytic CO₂ reduction, *J. Catal.* 413 (2022) 588–602, <https://doi.org/10.1016/j.jcat.2022.07.006>.
- [47] J. Wang, J. Zhang, S.B. Peh, G. Liu, T. Kundu, J. Dong, Y. Ying, Y. Qian, D. Zhao, Cobalt-containing covalent organic frameworks for visible light-driven hydrogen evolution, *Sci. China Chem.* 63 (2019) 192–197, <https://doi.org/10.1007/s11426-019-9658-1>.
- [48] Y. Guo, Y. Wang, Y. Shen, Z. Cai, Z. Li, J. Liu, J. Chen, C. Xiao, H. Liu, W. Lin, C. Wang, Tunable cobalt-polypyridyl catalysts supported on metal-organic layers for electrochemical CO₂ reduction at low overpotentials, *J. Am. Chem. Soc.* 142 (2020) 21493–21501, <https://doi.org/10.1021/jacs.0c10719>.
- [49] Paola Corio, Joel C. Rubim, Surface-enhanced Raman spectroscopic study of the adsorption and reduction of [M (bipy)₃]²⁺ complexes (M = Co, Ni) on a silver electrode, *J. Phys. Chem.* 99 (1995) 13217–13223, <https://doi.org/10.1021/j100035a028>.
- [50] E. Castellucci, et al., IR and Raman spectra of A 2,2'-bipyridine single crystal: internal modes, *Chem. Phys.* 43 (1979) 365–373, [https://doi.org/10.1016/0301-0104\(79\)85204-0](https://doi.org/10.1016/0301-0104(79)85204-0).
- [51] S. Wu, D. Wu, D. Zhang, W. Liu, H. Luo, J. He, Q. Yang, Z. Li, R. Liu, Boosting the activity and stability with dual-metal-N couplings for Li-O₂ battery, *Energy Environ. Mater.* 5 (2021) 918–927, <https://doi.org/10.1002/eem2.12210>.
- [52] L. He, K. Shi, Y. Pan, J. Wu, X. Li, X. Xin, Dual-functional 3D carbon fibers decorated with Co nanoparticles and Co-N_x sites for rechargeable aprotic Li-O₂ batteries, *N. J. Chem.* 46 (2022) 11570–11578, <https://doi.org/10.1039/D2NJ00970F>.
- [53] X. Yang, G. Xia, J. Ye, W. Du, Z. Zheng, A. Zhang, X. Li, C. Chen, C. Hu, High-content Co-N_x sites on carbon nanotubes for effective sulfur catalysis in lithium-sulfur batteries, *Appl. Surf. Sci.* 541 (2021), 148632, <https://doi.org/10.1016/j.apsusc.2020.148632>.
- [54] L. Peng, Y. Sun, S. Guo, C. Li, Highly efficient construction of hollow Co-N_x nanocube cage dispersion implanted with porous carbonized nanofibers for Li-O₂ batteries, *J. Mater. Chem. A* 10 (2022) 740–751, <https://doi.org/10.1039/D2TA90021A>.
- [55] L. Yang, H. Li, Y. Yu, Y. Wu, L. Zhang, Assembled 3D MOF on 2D nanosheets for self-boosting catalytic synthesis of N-doped carbon nanotube encapsulated metallic Co electrocatalysts for overall water splitting, *Appl. Catal. B: Environ.* 271 (2020), 118939, <https://doi.org/10.1016/j.apcatb.2020.118939>.
- [56] X. Hu, X.-J. Zheng, Y. Li, D.-K. Ma, Bipyridine-Co²⁺ molecular catalyst modified WO₃ nanoplate arrays photoanode with enhanced photoelectrochemical activity, *Mater. Lett.* 220 (2018) 36–39, <https://doi.org/10.1016/j.matlet.2018.02.109>.
- [57] Y. Xu, H. Zhang, J. Song, D. Wang, X. Gu, Boosting the on-demand hydrogen generation from aqueous ammonia borane by the visible-light-driven synergistic electron effect in antenna-reactor-type catalysts with plasmonic copper spheres and noble-metal-free nanoparticles, *Chem. Eng. J.* 401 (2020), 126068, <https://doi.org/10.1016/j.cej.2020.126068>.
- [58] Z. Peng, S.A. Freunberger, L.J. Hardwick, Y. Chen, V. Giordani, F. Barde, P. Novak, D. Graham, J.M. Tarascon, P.G. Bruce, Oxygen reactions in a non-aqueous Li⁺ electrolyte, *Angew. Chem. Int. Ed. Engl.* 50 (2011) 6351–6355, <https://doi.org/10.1002/ange.201100879>.
- [59] Cormac O. Laoire, Sanjeev Mukerjee, K.M. Abraham, Edward J. Plichta, Marry A. Hendrickson, Influence of nonaqueous solvents on the electrochemistry of oxygen in the rechargeable lithium-air battery, *J. Phys. Chem. C* 114 (2010) 9178–9186, <https://doi.org/10.1021/jp102019y>.
- [60] Y. Sasaki, H. Kato, A. Kudo, [Co(bpy)₃]^{3+/2+} and [Co(phen)₃]^{3+/2+} electron mediators for overall water splitting under sunlight irradiation using Z-scheme photocatalyst system, *J. Am. Chem. Soc.* 135 (2013) 5441–5449, <https://doi.org/10.1021/ja400238r>.
- [61] H. Kumagai, R. Aoyagi, K. Kato, A. Yamakata, M. Kakihana, H. Kato, Utilization of perovskite-type oxynitride La_{0.5}Sr_{0.5}Ta_{0.5}Ti_{0.5}O₂N as an O₂-evolving photocatalyst in Z-scheme water splitting, *ACS Appl. Energy Mater.* 4 (2021) 2056–2060, <https://doi.org/10.1021/acsaem.0c03055>.
- [62] Q. Yu, S. Ye, In situ study of oxygen reduction in dimethyl sulfoxide (DMSO) solution: a fundamental study for development of the lithium-oxygen battery, *J. Phys. Chem. C* 119 (2015) 12236–12250, <https://doi.org/10.1021/acs.jpcc.5b03370>.
- [63] M. Giannouri, M. Bidikoudi, L.M. Pastrana-Martínez, et al., Reduced graphene oxide catalysts for efficient regeneration of cobalt-based redox electrolytes in dye-sensitized solar cells, *Electrochim. Acta* 219 (2016) 258–266, <https://doi.org/10.1016/j.electacta.2016.10.013>.
- [64] Y. Zhang, X. Zhang, J. Wang, W.C. McKee, Y. Xu, Z. Peng, Potential-dependent generation of O^{2•-} and LiO₂ and their critical roles in O₂ reduction to Li₂O₂ in aprotic Li-O₂ batteries, *J. Phys. Chem. C* 120 (2016) 3690–3698, <https://doi.org/10.1021/acs.jpcc.5b12338>.
- [65] L. Johnson, C. Li, Z. Liu, Y. Chen, S.A. Freunberger, P.C. Ashok, B.B. Praveen, K. Dholakia, J.M. Tarascon, P.G. Bruce, The role of LiO₂ solubility in O₂ reduction in aprotic solvents and its consequences for Li-O₂ batteries, *Nat. Chem.* 6 (2014) 1091–1099, <https://doi.org/10.1038/nchem.2101>.
- [66] J. Lu, Y.J. Lee, X. Luo, K.C. Lau, M. Asadi, H.H. Wang, S. Brombosz, J. Wen, D. Zhai, Z. Chen, D.J. Miller, Y.S. Jeong, J.B. Park, Z.Z. Fang, B. Kumar, A. Salehi-Khojin, Y.K. Sun, L.A. Curtiss, K. Amine, A lithium-oxygen battery based on lithium superoxide, *Nature* 529 (2016) 377–382, <https://doi.org/10.1038/nature16484>.
- [67] R. Cao, Y. Cui, G. Huang, W. Liu, J. Liu, X. Zhang, Designing a photo-assisted Co₃N₄ cathode for high performance Li-O₂ batteries, *Nano Res.* (2022) 1–6, <https://doi.org/10.1007/s12274-022-5300-8>.
- [68] S. Zhou, Z. Xiao, Q. Yang, X. Huang, Y. Niu, Y. Ma, L. Zhi, Atomic cobalt anchored on covalent triazine frameworks with ultra-high performance towards oxygen reduction reaction, *Sci. China Mater.* 64 (2021) 2221–2229, <https://doi.org/10.1007/s40843-020-1609-9>.
- [69] F. Li, M.L. Li, H.F. Wang, X.X. Wang, L.J. Zheng, D.H. Guan, L.M. Chang, J.J. Xu, Y. Wang, Oxygen vacancy-mediated growth of amorphous discharge products toward an ultrawide band light-assisted Li-O₂ batteries, *Adv. Mater.* 34 (2022), 2107826, <https://doi.org/10.1002/adma.202107826>.
- [70] Y. Gu, Y. Ma, L. Wei, Y. Lian, Y. He, Y. Su, X. Li, Y. Peng, Z. Deng, Conformal lithium peroxide growth kinetically driven by MoS₂/MoN heterostructures towards high-performance Li-O₂ batteries, *Batter. Supercaps* 5 (2022), 202200222, <https://doi.org/10.1002/batt.202200222>.
- [71] Z. Lyu, L. Yang, Y. Luan, X. Renshaw Wang, L. Wang, Z. Hu, J. Lu, S. Xiao, F. Zhang, X. Wang, F. Huo, W. Huang, Z. Hu, W. Chen, Effect of oxygen adsorbability on the control of Li₂O₂ growth in Li-O₂ batteries: implications for cathode catalyst design, *Nano Energy* 36 (2017) 68–75, <https://doi.org/10.1016/j.nanoen.2017.04.022>.
- [72] W. Liu, Y. Yang, X. Hu, Q. Zhang, C. Wang, J. Wei, Z. Xie, Z. Zhou, Light-assisted Li-O₂ batteries with lowered bias voltages by redox mediators, *Small* 18 (2022), 2200334, <https://doi.org/10.1002/sml.202200334>.
- [73] Y. Feng, H. Xue, T. Wang, H. Gong, B. Gao, W. Xia, C. Jiang, J. Li, X. Huang, J. He, Enhanced Li₂O₂ decomposition in rechargeable Li-O₂ battery by incorporating WO₃ nanowire array photocatalyst, *ACS Sustain. Chem. Eng.* 7 (2019) 5931–5939, <https://doi.org/10.1021/acssuschemeng.8b05944>.
- [74] U. Sahapatombut, H. Cheng, K. Scott, Modelling the micro-macro homogeneous cycling behaviour of a lithium-air battery, *J. Power Sources* 227 (2013) 243–253, <https://doi.org/10.1016/j.jpowsour.2012.11.053>.
- [75] D. Su, D. Han Seo, Y. Ju, Z. Han, K. Ostrikov, S. Dou, H.-J. Ahn, Z. Peng, G. Wang, Ruthenium nanocrystal decorated vertical graphene nanosheets@Ni foam as highly efficient cathode catalysts for lithium-oxygen batteries, *NPG Asia Mater.* 8 (2016) 286, <https://doi.org/10.1038/am.2016.91>.
- [76] P. Hartmann, C.L. Bender, J. Sann, A.K. Durr, M. Jansen, J. Janek, P. Adelhelm, A comprehensive study on the cell chemistry of the sodium superoxide (NaO₂) battery, *Phys. Chem. Chem. Phys.* 15 (2013) 11661–11672, <https://doi.org/10.1039/C3CP50930C>.
- [77] K.U. Schwenke, M. Metzger, T. Restle, M. Piana, H.A. Gasteiger, The influence of water and protons on Li₂O₂ crystal growth in aprotic Li-O₂ cells, *J. Electrochem. Soc.* 162 (2015) A573–A584, <https://doi.org/10.1149/2.0201504jes>.
- [78] H. Wu, W. Sun, J. Shen, D.W. Rooney, Z. Wang, K. Sun, Role of flower-like ultrathin Co₃O₄ nanosheets in water splitting and non-aqueous Li-O₂ batteries, *Nanoscale* 10 (2018) 10221–10231, <https://doi.org/10.1039/C8NR02376J>.
- [79] Q. Yu, Q. Yu, W. Sun, H. Wu, Z. Wang, D. Rooney, K. Sun, Novel Ni@Co₃O₄ web-like nanofiber arrays as highly effective cathodes for rechargeable Li-O₂ batteries, *Electrochim. Acta* 220 (2016) 654–663, <https://doi.org/10.1016/j.electacta.2016.10.131>.